AE 460 Laboratory Report for Experiment 6

Design Lab

by

Luke Brown, Aaliyah Gaffey, Sara McCarthy, Ashley Sawa, and Aadit Kolar

TA: Nissrine Aziz

Section AB7, Group A, Wednesday 9 am

10 December, 2025

ABSTRACT

This experiment evaluated the aerodynamic performance of a blended-wing-body (BWB) aircraft designed for small payload delivery. The primary objectives were to design a BWB aircraft, predict its aerodynamic characteristics through theoretical analysis, and analyze the scaled down model's aerodynamic performance across a range of Reynolds numbers. The model, based on a small payload delivery drone, was designed in Siemens NX, manufactured with a Bambu X1 Carbon 3D printer, and tested in a low-speed wind tunnel, which uses a three-component sting balance, calibrated static-pressure ring, and an Omega PX653 pressure transmitter to record forces, moments, and freestream conditions. Measurements were collected from $-6°$ to $27°$ angle of attack in increments of three degrees, with freestream velocities of 25, 50, and 80 ft/s. These velocities correspond to Reynolds numbers of approximately 1.6×10^4 to 4.9×10^4. The theoretical performance was then predicted using Athena Vortex Lattice (AVL), which provided predictions of C_L, C_D, and C_m based on the model's sweep, twist distribution, and use of NACA 24-series airfoils. Wind-tunnel results showed that the lift coefficient increased linearly with angle of attack up to approximately 8° to 15°, depending on the wind tunnel speed. The measured drag coefficients were higher and more linear than the AVL predictions, whereas the pitching-moment coefficient closely matched the AVL coefficient and remained nearly constant with α, indicating that the neutral point was accurately predicted. Lastly, the drag polar demonstrated the expected quadratic relationship with C_L. Aside from the test condition of 25 ft/s, the wind tunnel data had close correspondence with the AVL analysis. Additional analysis found that the measured normal and axial forces increased consistently with angle of attack, with the largest values at higher velocities due to higher dynamic pressure. A comparison between the theoretical and experimental data showed the limitations of inviscid vortex-lattice methods at low Reynolds numbers. Using the nondimensional coefficients measured in the tunnel, these results suggest that a full-scale version of this aircraft could achieve an estimated lift of 5 to 11 pounds under realistic material and structural assumptions. Overall, this experiment demonstrated that the BWB configuration produced stable pitching behavior and generated aerodynamic forces consistent with the theoretical analysis, suggesting that a scaled-up version could support a viable drone design.

1 INTRODUCTION

Unlike conventional tube-and-wing aircraft, BWB aircraft integrate the fuselage with the wing to form a single lifting surface, which distributes lift more efficiently across the entire planform, reduces the wetted area and structural weight and improves fuel economy and payload capacity. These advantages make BWBs suitable for long-range transport, high-capacity passenger aircraft, and low-emission aircraft.

Early investigations into BWB aircraft date back to the 1920s, with the first being the

Westland Dreadnaught. However, the vehicle crashed on its first flight and severely injured the test pilot [1]. Renewed interest emerged in the 1990s as NASA and McDonnell Douglas evaluated the use of a BWB for commercial transport applications. This partnership resulted in a 6% scale model named the BWB-17, which had stable aerodynamic properties [2]. Following the successful testing of the BWB-17, programs shifted their focus to understanding the BWB aerodynamics and its applications for sustainable aviation. NASA and Boeing's X-48 series of subscale vehicles demonstrated that BWB platforms could achieve reduced emissions, fuel burn, and noise [3]. Outside of sustainable aviation, BWBs are also under study for use in autonomous cargo missions, surveillance roles, and long-range missions.

In this experiment, we designed, manufactured, and tested a subscale BWB model tailored to small unmanned-aircraft applications. The inspiration for the design is based on Natilus' *Kona* drone and Zipline's blood-delivery drones in Rwanda [4, 5]. The objective was to determine whether a BWB drone could offer favorable aerodynamic performance and be used for future air-medical operations.

This experiment involved designing and fabricating a scaled BWB drone model for wind-tunnel evaluation. The model was tested at freestream velocities of 25, 50, and 80 ft/s over a range of angles of attack from -6° to 27° in increments of 3°. For each test condition, normal force, axial force, and pitching moment were measured and subsequently converted into lift, drag, and moment coefficients. These data were used to construct lift curves, drag polars, and pitching-moment trends. The resulting aerodynamic characteristics provided the basis for assessing whether a full-scale version of the concept could meet the performance requirements of the intended mission.

2 THEORY AND ANALYSIS

A	Axial force measured by balance [lbf]
N	Normal force measured by balance [lbf]
M_{bal}	Pitching moment about balance center [in-lbf]
α	Angle of attack [deg] or [rad]
L	Lift force [lbf]
D	Drag force [lbf]
q_∞	Freestream dynamic pressure, $144\, q_{\text{corr}}$ [psf]
q_{corr}	Differential pressure from transducer [psi]
S	Wing reference area [ft^2]
$\bar{c}$	Mean aerodynamic chord [in]
V	Freestream velocity [ft/s]
ρ	Freestream air density [slug/ft^3]
μ	Dynamic viscosity [slug/(ft·s)]
Re	Reynolds number, $\rho V \bar{c}/\mu$
C_L	Lift coefficient, $L/(q_\infty S)$
C_D	Drag coefficient, $D/(q_\infty S)$
C_m	Pitching-moment coefficient about neutral point
$C_{M,\text{bal}}$	Pitching-moment coefficient about balance center
x_{ref}	Moment reference point (nose → balance reference) [in]
x_{NP}	Neutral point location measured from nose [in]
dx	Offset $x_{\text{ref}} - x_{NP}$ used for moment-shift correction [in]
C_{D0}	Parasite drag coefficient in drag polar
k	Induced drag factor in drag polar

The aerodynamic quantities used in this experiment are obtained by converting the raw measurements from the three-component sting balance into nondimensional aerodynamic coefficients. These coefficients allow for meaningful comparison between tests at different flow speeds and enable direct evaluation of the blended-wing-body design. The equations below describe the theory applied in the analysis and match the exact computational steps implemented in the data-processing code.

The sting balance provides the normal force N, axial force A, and pitching moment M_{bal} about the balance center. These forces are measured in the balance coordinate system and must be rotated into the wind-axis system using the measured angle of attack α. Assuming zero sideslip and alignment with the freestream, the lift L and drag D are computed as

$$L = N\cos\alpha - A\sin\alpha, \tag{1}$$

$$D = N\sin\alpha + A\cos\alpha. \tag{2}$$

Dynamic pressure q_∞ is obtained from the corrected differential pressure measurement. Since the pressure transducer outputs psi, the conversion to psf is performed using the factor 144:

$$q_\infty = 144\, q_{\text{corr}}. \tag{3}$$

Using the reference wing area S and mean aerodynamic chord $\bar{c}$, the nondimensional lift and drag coefficients are defined as

$$C_L = \frac{L}{q_\infty S}, \tag{4}$$

$$C_D = \frac{D}{q_\infty S}. \tag{5}$$

The pitching moment measured by the balance is referenced to the balance center, which is located 0.62 inches aft of the setscrew. Adding this offset to the distance from the nose of the aircraft to the setscrew yields a total reference moment-arm location of

$$x_{\text{ref}} = 2.12 \text{ in.}$$

The pitching moment coefficient about the balance center is computed as

$$C_{M,\text{bal}} = \frac{M_{\text{bal}}}{q_\infty S \bar{c}}. \tag{6}$$

The final pitching-moment coefficient must be referenced to the aircraft's neutral point x_{NP}, which is determined experimentally for each wind-tunnel speed. Applying the standard aerodynamic moment-shift relation yields

$$C_m = C_{M,\text{bal}} - \left(\frac{x_{\text{ref}} - x_{NP}}{\bar{c}} \right) C_L. \tag{7}$$

Equation (7) is implemented exactly in the analysis code by defining

$$dx = x_{\text{ref}} - x_{NP},$$

and subtracting $(dx/\bar{c})C_L$ from $C_{M,\text{bal}}$. This correction ensures that the pitching-moment curves reflect the behavior of the aircraft relative to its neutral point rather than the arbitrary balance reference.

The Reynolds number, which represents the ratio of inertial to viscous forces, is defined by

$$Re = \frac{\rho V \bar{c}}{\mu}. \tag{8}$$

Finally, the relationship between drag and lift is compared against the theoretical parabolic drag polar,

$$C_D = C_{D0} + k C_L^2, \tag{9}$$

where C_{D0} represents parasitic drag and k characterizes induced drag. Because AVL is inviscid, discrepancies between its predictions and the measured drag are expected, especially at the low Reynolds numbers of this experiment.

3 APPARATUS

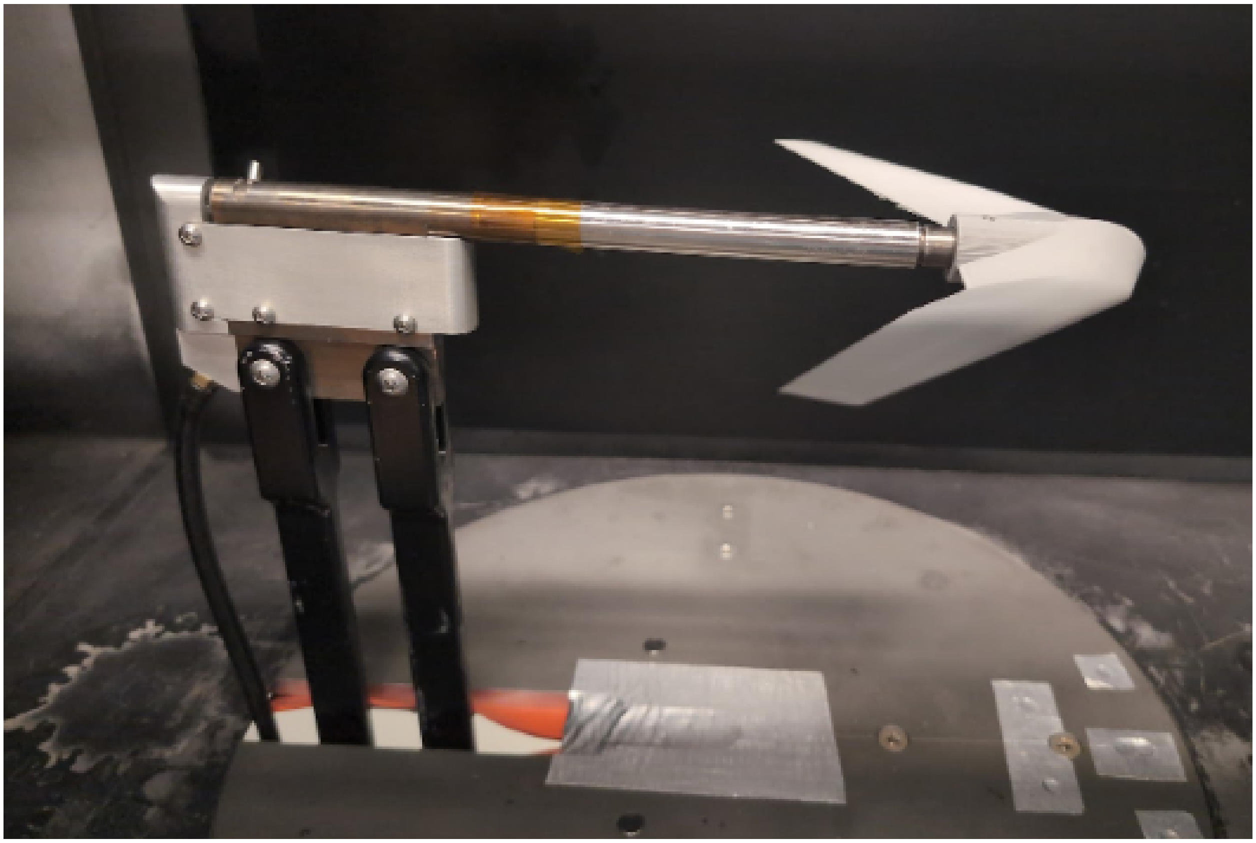

Figure 1: Model mounted on the Sting Balance

The model is correctly mounted on the three-component sting balance and screwed into place with help from the TA, as seen in Fig. 1. The model is angled to the first angle of attack and the wind tunnel brought up to the RPM that correlates to the correct velocity. All instruments activate and collect data to send to the computer. A detailed list of the laboratory instruments and their respective uses can be seen in Table 1 [6].

Number	Name of Item	Size, Range	Measurement Accuracy	Use in Experiment
1	Aerolab low-speed wind tunnel	Test Section: 24"x 12"x 12"	n/a	Contains test section for measurements
2	Static Pressure Ring	n/a	n/a	Collects the freestream velocity for calculations
3	Omega PX653 Pressure Transmitter 0 to ±10 in. W.C	±0.25%	Measures the dynamic pressure and velocity	
4	Data Acquisition	sampling rate of 100 kS/s	±25 mV/V	Collect data
5	Three-Component Sting Balance and Model-Positioning System	Normal Force max: 20 lbs, Axial Force max: 9 lbs, Pitching Moment max: 40 inch-lbs	±0.2 degrees, 5% for forces and moments	Angles the model for testing
6	Bambu X1 Carbon 3D Printer	256 x 256 x 256 mm	8 microns	Build the model
7	Personal computer with LabVIEW software	n/a	n/a	Combines data for collection

Table 1: Instrumentation in Lab 6

4 PROCEDURE

The model is mounted onto the sting balance and screwed into place with help from the TA. The test section is closed, and the tunnel tared out. The ambient pressure, temperature and chord length are inputted into LabView. The RPM is gradually increased until it hits approximately 25 ft/s. At that point, the model is brought down to the angle of -6 degrees, and data is taken. From there it goes up to 27 degrees, in 3 degree increments, with data taken at each increment (12 data points total). The data handwritten down includes the exact angle of attack, axial force, normal force, pitching moment and Reynolds number. With that velocity done, the steps are repeated for 50 ft/s and 80 ft/s.

5 EXPERIMENTAL UNCERTAINTY

Experimental uncertainty in this lab comes from uncertainty in the measurements of axial force, normal force, and angle of attack. From the lab manual we know that the axial and normal force measurements, along with the pitching moments are accurate within 5 percent. We also know that the angle of attack is accurate to within plus or minus 0.2 degrees. We can see the calculated experimental uncertainties for each of the coefficients in Table 2. Sample calculations are available in the appendix at 7 and .1.

Table 2: Lift, Drag, and Moment Coefficient Uncertainties at Different Airspeeds

Data Point	**25 ft/s**			**50 ft/s**			**80 ft/s**		
	σ_{C_L}	σ_{C_D}	σ_{C_M}	σ_{C_L}	σ_{C_D}	σ_{C_M}	σ_{C_L}	σ_{C_D}	σ_{C_M}
1	0.0083	0.0641	0.0718	0.0121	0.0167	0.0726	0.0122	0.0025	0.0754
2	0.0060	0.0659	0.0896	0.0040	0.0103	0.0106	0.0043	0.0021	0.0078
3	0.0077	0.0343	0.0537	0.0029	0.0054	0.0510	0.0066	0.0005	0.0643
4	0.0152	0.0124	0.0266	0.0109	0.0010	0.1102	0.0141	0.0025	0.1327
5	0.0221	0.0154	0.0244	0.0195	0.0050	0.1762	0.0223	0.0048	0.2018
6	0.0286	0.0339	0.0658	0.0271	0.0102	0.2325	0.0319	0.0074	0.2702
7	0.0366	0.0637	0.1146	0.0343	0.0173	0.2892	0.0392	0.0109	0.3290
8	0.0442	0.0867	0.1450	0.0393	0.0239	0.3371	0.0450	0.0144	0.3905
9	0.0566	0.1142	0.1799	0.0368	0.0277	0.2713	0.0406	0.0179	0.3604
10	0.0684	0.1294	0.2081	0.0359	0.0336	0.2210	0.0364	0.0201	0.2939
11	0.0824	0.1490	0.2331	0.0401	0.0386	0.2500	0.0355	0.0232	0.2628
12	0.0998	0.1645	0.2733	0.0450	0.0444	0.2714	0.0379	0.0267	0.2775

6 RESULTS AND DISCUSSION

6.1 Part 1: Description of Design

The aircraft developed for this project utilizes a flying wing design. The primary considerations during the design phase were pitch stability and aerodynamic efficiency. Reflexed airfoils were considered for their moment characteristics, but ultimately 4-series NACA airfoils were selected for their simplicity and flexibility.

As mentioned in Section 2, the aircraft must have a positive C_{m0} and negative $C_{m\alpha}$ to be longitudinally stable. To achieve this, the wing was swept back aggressively, with a leading edge sweep of greater than 50° for a majority of the span. Additionally, a twist distribution was added, going from 0° at the leading edge to -7° at the wingtip. This has the additional effect of delaying stall at the wingtips, meaning the aircraft pitches down when it stalls, aiding stall recovery. Both of these modifications result in the neutral point moving rearward, allowing a larger allowable CG range (range where it is ahead of the neutral point).

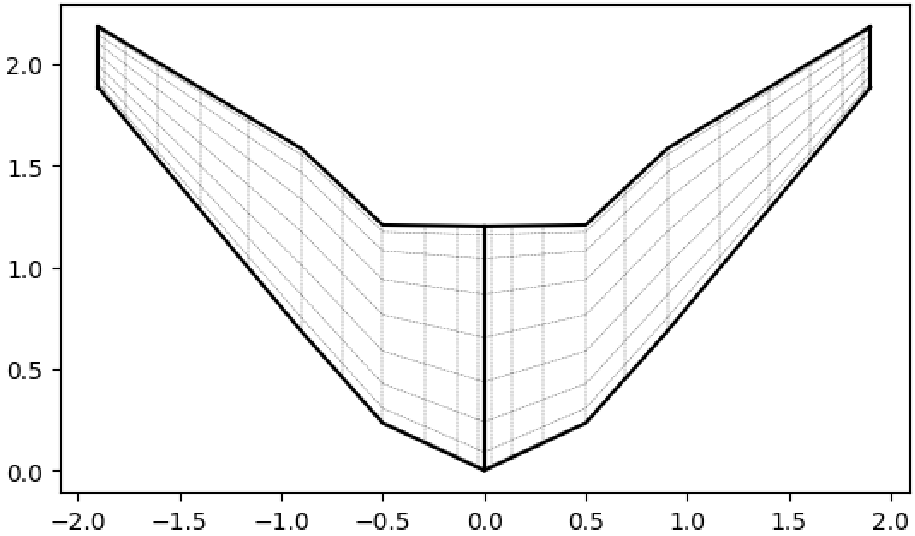

Figure 2: Full Size Aircraft Wing

The aircraft has a wingspan of 3.8 feet with a length of 2.2 feet. Its internal volume is 5.5 in^3. The inner section of the airframe from 0 to 0.5ft span uses a NACA 2440 airfoil to maximize internal payload volume. Storing the delivery payload internally means the airflow around the aircraft is not disrupted by external fairings, theoretically resulting in a more aerodynamically efficient design. The rest of the aircraft uses standard NACA 2420 and 2412 airfoils.

To test the aircraft in the wind tunnel, a 1:8 scale model was used. A mount was added at the rear of the aircraft to mount the sting balance, which was used to measure the forces and moments on the test model. Fig. 3 depicts an engineering sketch of the model

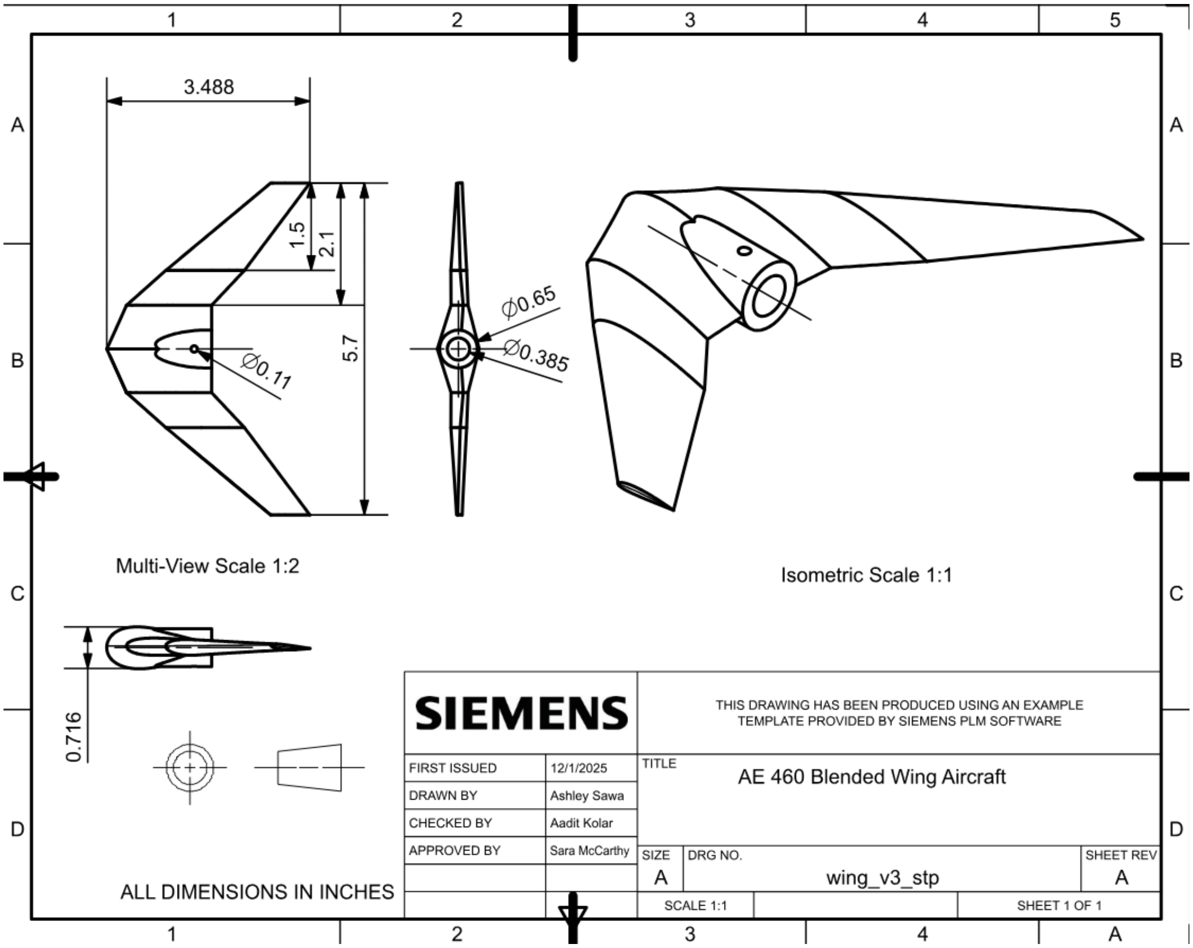

Figure 3: Engineering Sketch of the Model Aircraft

Fig 3 depicts the critical dimensions for the model, including its span and the length of each wing section. Additionally, it depicts the sting mount in the form of a circular extrusion on the back of the aircraft. The back of the aircraft proved too thin to effectively mount the sting via a single hole, so a mount was integrated into the design of the craft. A circle was extruded into the trailing edge of the aircraft and blended into the wing. The sting mounting hole and through hole for the mounting screw was then added to the extrusion. The mount was designed to result in minimal disturbances in order to ensure the accuracy of values collected via wind tunnel experimentation.

6.2 Part 2: Theoretical Analysis

To theoretically analyze the aerodynamics of the model, the wing geometry was inputted to AVL (Athena Vortex Lattice), a Vortex-Lattice method solver written by Mark Drela. Since the code is inviscid and cannot predict profile and skin friction drag, an additional estimated drag coefficient $C_{D0} = 0.08$ is added, using an estimation from Raymer's book on aircraft design [7]. AVL produces the following results:

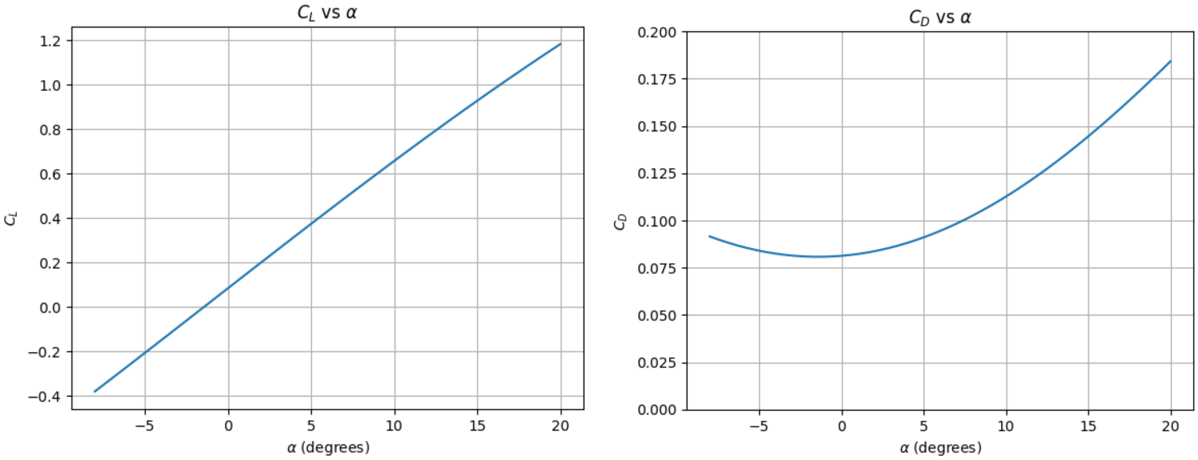

Figure 4: Lift and Drag Coefficients At Different Angles of Attack

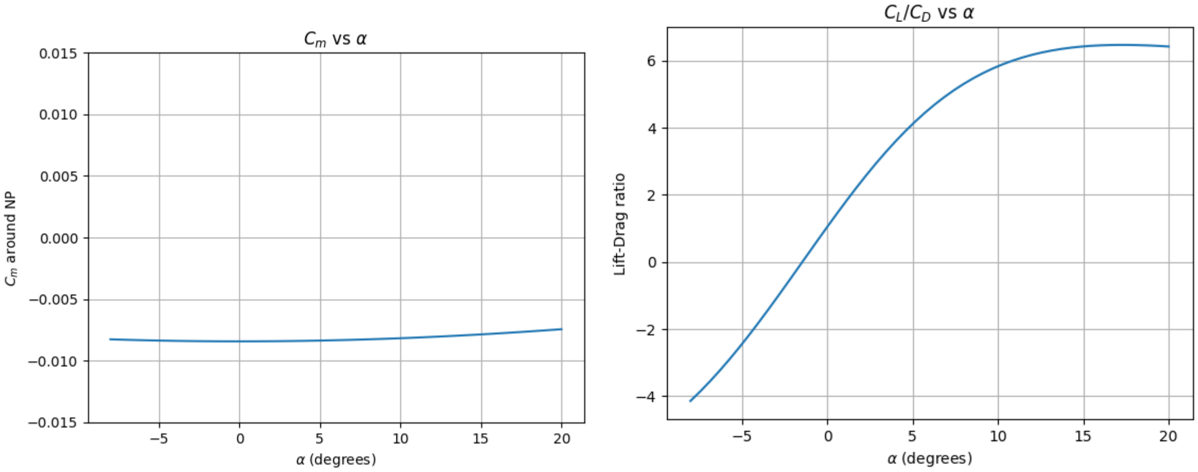

Figure 5: Moment Coefficient and Lift-Drag Ratio at Different Angles of Attack

As seen in Fig. 4, the lift coefficient C_L varies linearly with angle of attack α. Since AVL is an inviscid panel method, it cannot predict the wing's stall characteristics. The wing's C_L at $\alpha = 0$ is 0.084, and the slope of the line ($C_{L\alpha}$) is 3.19 per radian, which is much lower than a 2D airfoil's lift-curve slope of 2π. As expected, the aircraft's drag coefficient forms a parabola, as it is quadratically related to the lift coefficient: $C_D = C_{D0} + k{C_L}^2$.

Since the moment coefficient C_m is calculated around the Neutral Point of the aircraft, the moment around this point should not change with respect to α. This behavior is seen in the graph, where C_m stays roughly constant with α, varying by less than 0.002.

The lift-drag graph shows the lift-drag ratio increases with α, though the slope starts to reduce around $\alpha = 5°$, and it peaks at around $\alpha = 15°$ at a value of $\frac{L}{D}_{max} = 6.46$. For the real aircraft, it is unlikely the max lift-drag ratio would occur at such a high α since it is approaching or beyond the stall region of the wing.

6.3 Part 3: Tabulated Data

Using the data in Table 9, the values for Table 3 were determined, and an average Reynolds number of 15,882 (taken an average from data in Table 9).

Angle of Attack [deg]	**Axial Force [lbf]**	**Normal Force [lbf]**	**Pitching Moment [in-lbf]**
-6.03	-0.04	0.00	-0.01
-2.96	-0.05	0.00	-0.01
0.01	-0.02	0.01	0.00
3.04	-0.01	0.01	0.00
5.97	0.01	0.02	0.00
9.06	0.02	0.02	0.00
11.97	0.04	0.02	0.01
15.02	0.06	0.03	0.01
17.98	0.08	0.03	0.01
21.03	0.09	0.03	0.02
23.94	0.11	0.04	0.02
26.99	0.12	0.04	0.02

Table 3: Normal Force, Axial Force and Pitching Moment for 25 ft/s

The corresponding values from Table 4 were extracted, yielding an average Reynolds number of 31,741 (taken an average from data in Table 8).

Angle of Attack [deg]	Axial Force [lbf]	Normal Force [lbf]	Pitching Moment [in-lbf]
-6.04	-0.05	-0.03	-0.02
-2.98	-0.03	-0.01	0.00
0.04	-0.01	0.01	0.02
3.05	0.00	0.03	0.03
5.97	0.01	0.05	0.05
9.04	0.02	0.07	0.07
11.97	0.04	0.09	0.08
14.95	0.06	0.10	0.10
17.97	0.07	0.10	0.08
21.01	0.09	0.10	0.07
24.03	0.10	0.11	0.08
26.99	0.12	0.12	0.08

Table 4: Normal Force, Axial Force and Pitching Moment for 50 ft/s

Using data from Table 7, the values for Table 5 can be grabbed with the average Reynolds Number being 49344 (taken an average from data in Table 7).

Angle of Attack [deg]	Axial Force [lbf]	Normal Force [lbf]	Pitching Moment [in-lbf]
-6.03	-0.01	-0.09	-0.06
-2.96	-0.02	-0.03	-0.01
0.01	0.00	0.05	0.05
3.05	0.01	0.10	0.10
5.98	0.03	0.15	0.14
9.03	0.03	0.20	0.19
11.96	0.04	0.25	0.22
14.98	0.04	0.28	0.25
17.98	0.08	0.26	0.24
21.00	0.10	0.26	0.21
23.94	0.12	0.25	0.19
27.00	0.13	0.26	0.19

Table 5: Normal Force, Axial Force and Pitching Moment for 80 ft/s

6.4 Part 4: Neutral Point

On an aircraft, the neutral point is the location on the longitudinal axis where, as the angle of attack changes, the pitching moment remains constant. The neutral point on the model was estimated from wind tunnel data by first calculating the force of lift, where L is the force of lift, N is the normal force measured by the balance, α is the angle of attack, and A is the axial force measured by the balance.

$$L = N\cos\alpha - A\sin\alpha \tag{10}$$

The lift force is then used to determine the coefficient of lift, which is dependent on the wing reference area S and dynamic pressure q_∞. q_∞ changes based on the wind tunnel velocity V and air density ρ.

$$q_\infty = \tfrac{1}{2}\rho V^2 \tag{11}$$

$$C_L = \frac{L}{q_\infty S} \tag{12}$$

The pitching moment from the experimental data was nondimensionalized to obtain $C_{M,\mathrm{bal}}$, where $\bar{c}$ is the mean aerodynamic chord.

$$C_{M,\mathrm{bal}} = \frac{M_{\mathrm{bal}}}{q_\infty S\bar{c}} \tag{13}$$

To approximate the linear behavior from C_L and $C_{M,\mathrm{bal}}$, linear regressions were performed between the angle of attacks of -6 and 6 degrees. The slopes of the lift and pitching moment coefficients are written as a_{CL} and a_{CM}, respectively.

The neutral point location x_{NP} along the mean aerodynamic chord can be expressed in terms of the slopes of the lift and pitching moment coefficients, mean aerodynamic chord, and balance center location x_{bal}

$$x_{NP} = x_{\text{bal}} - \left(\frac{a_{CM}}{a_{CL}}\right)\bar{c} \tag{14}$$

This calculation is completed for each Reynolds number. The neutral point was also calculated with AVL (Athena Vortex Lattice), a software package that uses the model geometry to account for characteristics and planform and twist within an aircraft wing. The results can be seen in Table 6 relative to the leading edge.

Run	Average Reynolds Number, Re	Velocity (ft/s)	Neutral point, x_{NP} (in)	Neutral point, $x_{NP}/\bar{c}$
1	15,882.53	25	1.696	15.882%
2	31,741.13	50	1.243	11.634%
3	49,344.17	80	1.219	11.409%
AVL	N/A	N/A	1.328	12.434%

Table 6: Neutral point estimates from wind tunnel data & AVL.

As can be seen in Table 6, the 50 ft/s, 80 ft/s, and AVL neutral point values are quite similar, and the 1-1.5% discrepancy can be explained with experimental error and uncertainty. However, looking at the 25 ft/s value, the aircraft appears far more stable. This can be attributed to the small force and moment values obtained from the experiment, which are closer to the balance resolution and understandably have a higher amount of error. The noise in the data results in non-insignificant changes in the calculated slope values and therefore the neutral point. Given that the 50 ft/s, 80 ft/s, and AVL values agree with two different solving techniques (Reynolds via data and based on geometry), the neutral point of the aircraft is 1.219 to 1.328 inches from the leading edge.

6.5 Part 5: Aerodynamic Data Analysis and Comparison with Theoretical Predictions from AVL

Aerodynamic Data Analysis

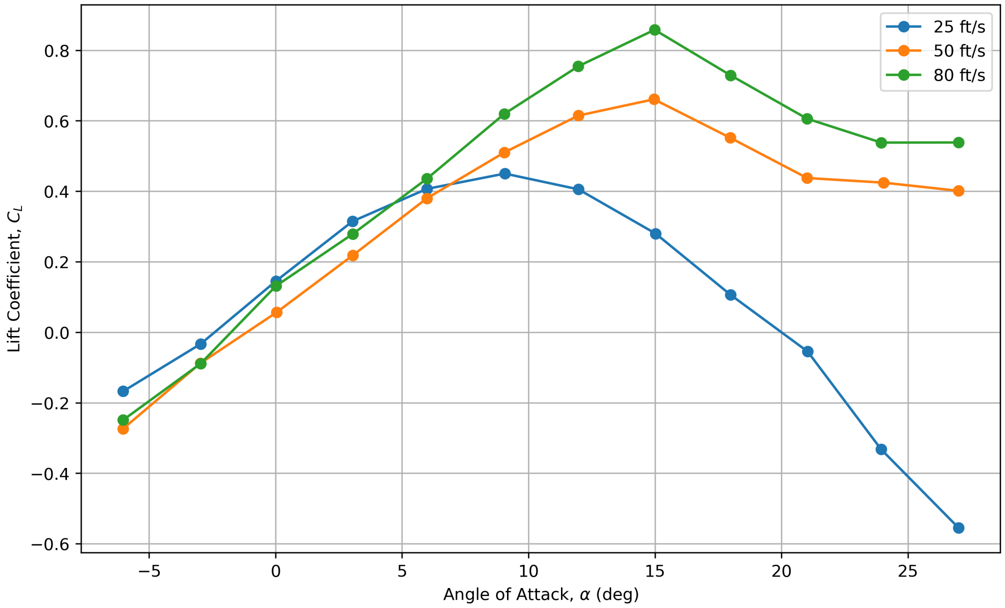

Figure 6: C_L **vs.** α

Figure 6 shows that the lift coefficient increases nearly linearly with angle of attack for all three tunnel speeds. The slope becomes steeper as Reynolds number increases, and the 80 ft/s case reaches the largest peak C_L before stall. At 25 ft/s, the lift curve turns over more abruptly near $\alpha \approx 12°$, indicating earlier flow separation due to the significantly lower Reynolds number. The 50 and 80 ft/s curves stall more gradually and retain lift longer, suggesting that the twist distribution and swept-wing geometry help soften the stall behavior at higher speeds.

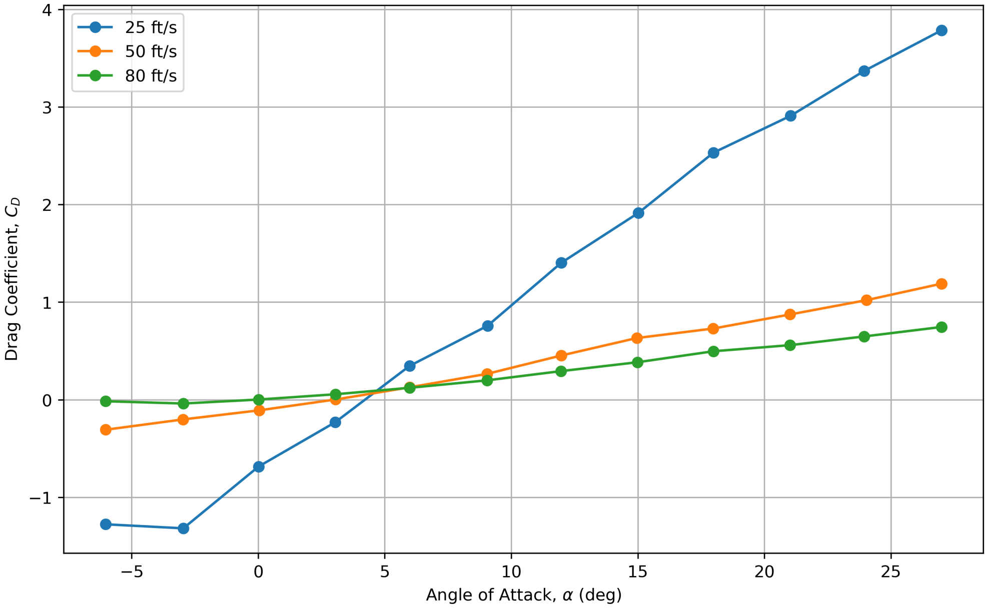

Figure 7: C_D **vs.** α

Figure 7 displays the drag coefficient as a function of angle of attack. Drag increases monotonically with α for the 50 and 80 ft/s data, following the expected trend of increasing pressure drag and induced drag. At 25 ft/s, however, the small magnitude of axial force results in noticeable measurement scatter and even slightly negative values at low angles, which are not physically meaningful but are typical when forces approach the resolution limits of the balance. Once the angle of attack increases and the forces grow, the 25 ft/s curve aligns more closely with the higher-speed trends.

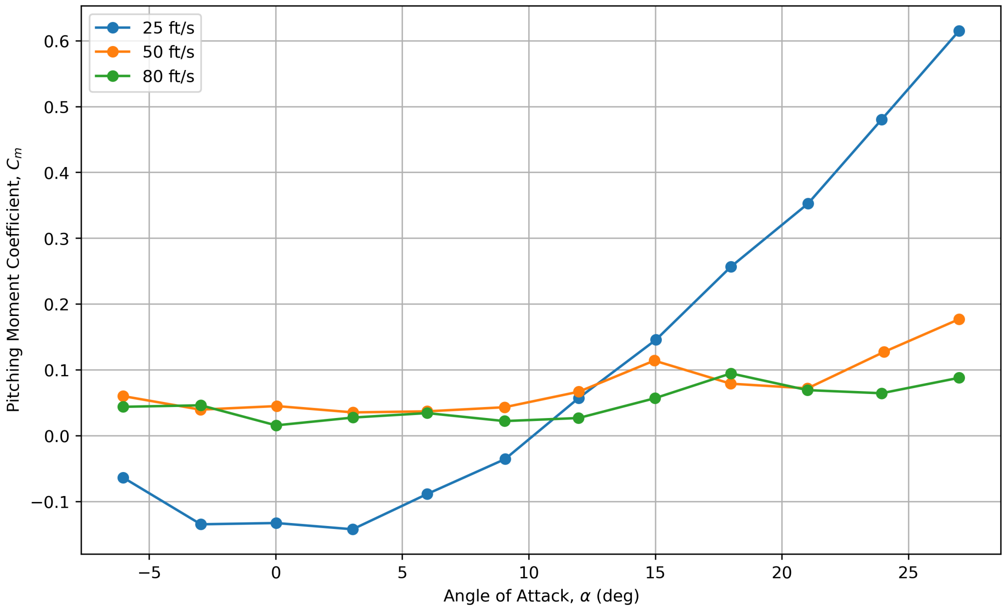

Figure 8: C_m vs. α referenced to the neutral point

The pitching-moment behavior shown in Fig. 8 reflects the moment-shift correction applied to reference all data to the neutral point. For 50 and 80 ft/s, the moment coefficient remains nearly constant with angle of attack, as expected at the neutral point where the slope $\partial C_m/\partial\alpha$ should approach zero. The 25 ft/s curve exhibits more variation because the small measured moments are highly sensitive to noise and balance resolution. The consistency of the higher-speed results supports the neutral-point estimates reported earlier and indicates that the model achieves the near-neutral longitudinal stability intended in its design.

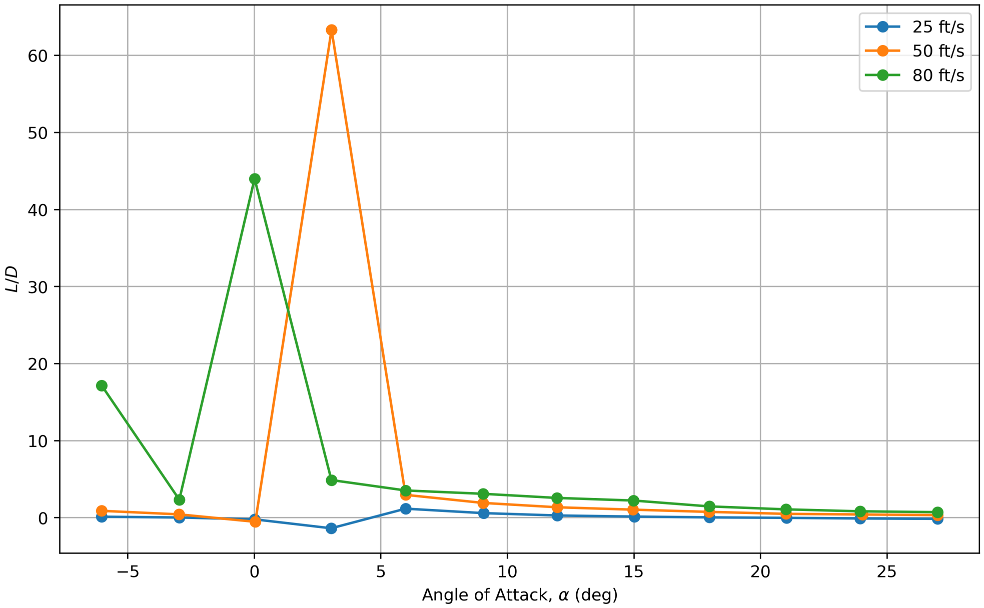

Figure 9: L/D **vs.** α

As shown in Fig.9, the lift-to-drag ratios show large variability at low angles of attack, particularly at 50 ft/s and 80 ft/s, where individual data points produce unrealistically high L/D values. These spikes likely indicate measurement noise or force-balance errors at small lift values, rather than true aerodynamic performance. Beyond approximately 5 degrees, all three speeds converge to similar L/D trends, suggesting that the model behaves more consistently at moderate angles of attack where forces are larger and measurements are more reliable.

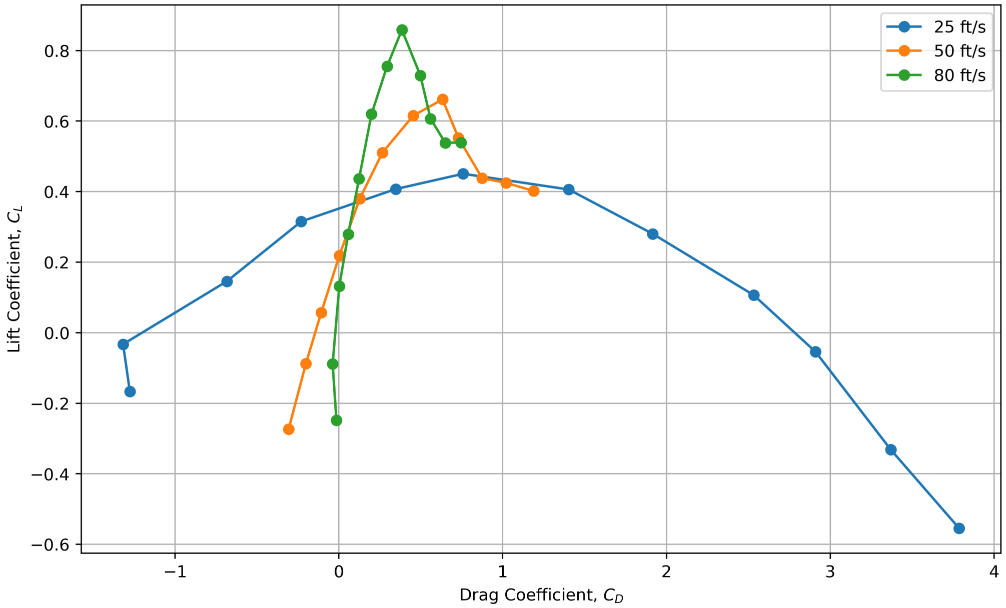

Figure 10: Drag polar: C_L vs. C_D

The drag polar in Fig. 10 provides a combined view of aerodynamic efficiency. The 50 and 80 ft/s data form a smooth parabolic curve characteristic of the classical drag polar relation $C_D = C_{D0} + kC_L^2$. The 80 ft/s polar shows the highest aerodynamic efficiency and the largest operating envelope. The 25 ft/s curve departs from this parabolic shape at low lift values due to the same measurement limitations discussed earlier, but converges toward the expected trend once the forces become sufficiently large. Overall, the data shows that the tests at higher velocities produce cleaner, more consistent aerodynamic behavior, while the lowest-speed run is dominated by viscous effects and instrumentation noise.

Comparison with Theoretical Predictions from AVL

In comparison with the data taken from the wind tunnel, AVL produces more linear, smooth coefficient plots because it neglects viscous effects, separation, and Reynolds-number dependence, while the wind-tunnel results reflect the combined influence of geometry, viscosity, and measurement limitations.

For the lift coefficient, AVL predicts a strictly linear relationship between C_L and α, with a modest lift-curve slope and no stall behavior. The experimental results follow this trend at low angles of attack, particularly for the 50 and 80 ft/s runs, which exhibit linear lift growth consistent with the AVL slope. However, the measured slopes are slightly lower than the AVL prediction, especially at 25 ft/s, where viscous effects and low Reynolds numbers reduce lift production. The experimental curves also show clear stall behavior between 12 and 18 degrees depending on tunnel speed, which AVL cannot capture. This difference is expected and highlights the limitations of inviscid theory for predicting nonlinear aerodynamic behavior.

The drag coefficient shows the greatest discrepancy between AVL and experiment, as AVL can only reproduce the induced-drag component and requires an assumed parasite drag value. While the AVL curves produce a smooth parabolic increase in C_D with C_L, the experimental data reveal higher drag levels across all angles of attack, especially at 25 ft/s where the boundary layer is more prone to separation. At 50 and 80 ft/s, however, the parabolic shape predicted by AVL is closely mirrored by the measured drag polar, and the 80 ft/s data show the cleanest overall agreement once parasite drag and viscous effects are considered. This convergence indicates that the model geometry behaves largely as AVL predicts at moderate Reynolds numbers, with deviations arising from real-world viscous losses.

The moment coefficient comparison further illustrates the differences between inviscid and experimental behavior. AVL predicts an almost perfectly constant pitching-moment coefficient referenced to the neutral point, consistent with theory. The experimental results at 50 and 80 ft/s align well with this expectation: C_m varies only slightly with angle of attack, demonstrating that the model behaves near its neutral point and that the geometry-driven stability characteristics are captured accurately by AVL. At 25 ft/s, the pitching-moment curve exhibits more variability, reflecting the influence of small force magnitudes relative to balance resolution. The agreement at higher speeds suggests that AVL provides a reliable estimate of the aircraft's longitudinal stability characteristics when Reynolds-number effects are less dominant.

Taken together, the comparison shows that AVL captures the fundamental aerodynamic trends of the blended-wing-body configuration, particularly the linear lift response, the parabolic drag polar shape, and the near-constant pitching moment about the neutral point. Deviations in the experimental data, most notably early stall, elevated drag, and increased scatter at low speeds, arise from viscous effects and measurement limitations that AVL does not model. As Reynolds number increases, the wind-tunnel results approach AVL predictions more closely, reinforcing the value of combining inviscid analysis with experimental data to assess the aerodynamics of low-speed blended-wing configurations.

6.6 Part 6: Full-Scale Aircraft

Given the wind tunnel data obtained from the scale model, the feasibility of the full-scale aircraft can now be examined. It is useful to first note the full-scale geometry as it compares to the wind tunnel model. The wind tunnel model is slightly less than one eighth of the size of the full-scale aircraft, with the model's mean aerodynamic chord being 1.31 inches, and the full-scale mean aerodynamic chord being 10.68 inches. The model's wingspan is 5.7 inches, and the full-scale wingspan is approximately 3.8 feet. From the CAD file, the volume of the full-scale model is found to be 796.7 in^3, and the wing planform area is approximately 8.544 ft^2.

The full-scale aircraft would likely fly at similar mach numbers to the wind tunnel model, as the full-scale will fly at relatively low altitudes and therefore similar atmospheric conditions to the model. Additionally, the full-scale likely will not fly any faster than the fastest test speed of 80 ft/s.

The Reynolds numbers for the full-scale aircraft will be considerably larger than those seen in the wind tunnel test, with the predicted numbers being roughly 131085, 262170, and 419472 for air speeds of 25 m/s, 50 m/s, and 80 m/s respectively. These numbers are roughly

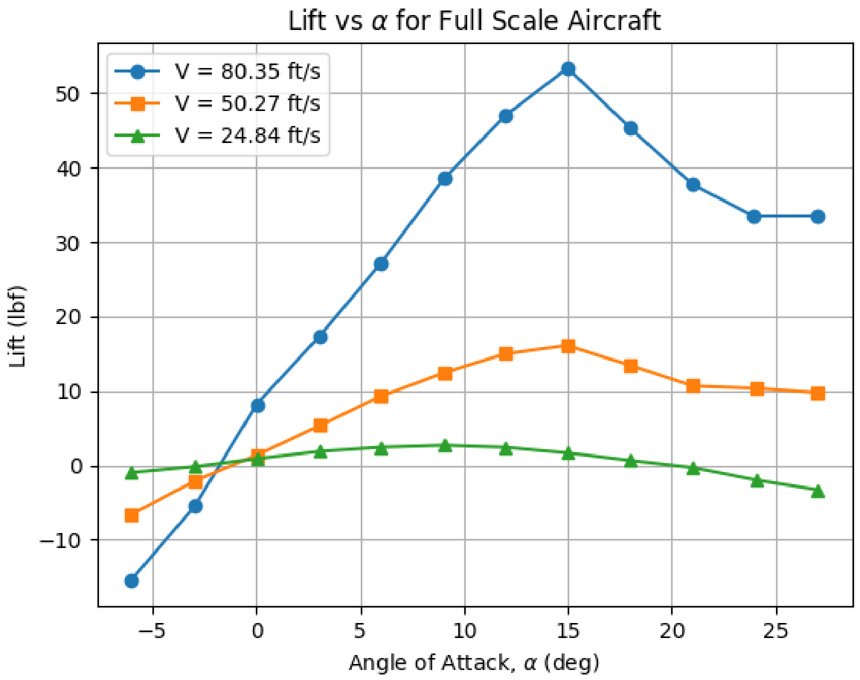

Figure 11: Predicted Lift versus Angle of Attack for the full-scale Aircraft

10 times larger than the model numbers at the same speeds. This means that the full-scale aircraft will be less susceptible to boundary layer and viscous effects, and will likely perform better than predicted.

In order to estimate the mass properties of the full-scale aircraft material choice first needs to be examined. Reasonable material choices for an aircraft of this size would be a carbon fiber composite skin with a foam core. While there would be additional mass from the needed electronic components, this can be accounted for by using high end estimates for structural materials. From carbon fiber producer Toray, we can see that carbon fiber has a density of 1.76 g/cm^3, which is approximately 110 lb/ft^3 [8]. To account for resin used to make a carbon fiber composite, we will opt to use a high end density estimate of 200 lb/ft^3. We will assume that polystyrene foam will be used as an internal wing structure to provide shape to our wing. A foam core wing is common for small scale UAVs. From foam manufacturer Foam Factory, we can find that expanded polystyrene (EPS) can be obtained in many different densities. For our estimates we will opt for 2 lb foam, which has a density

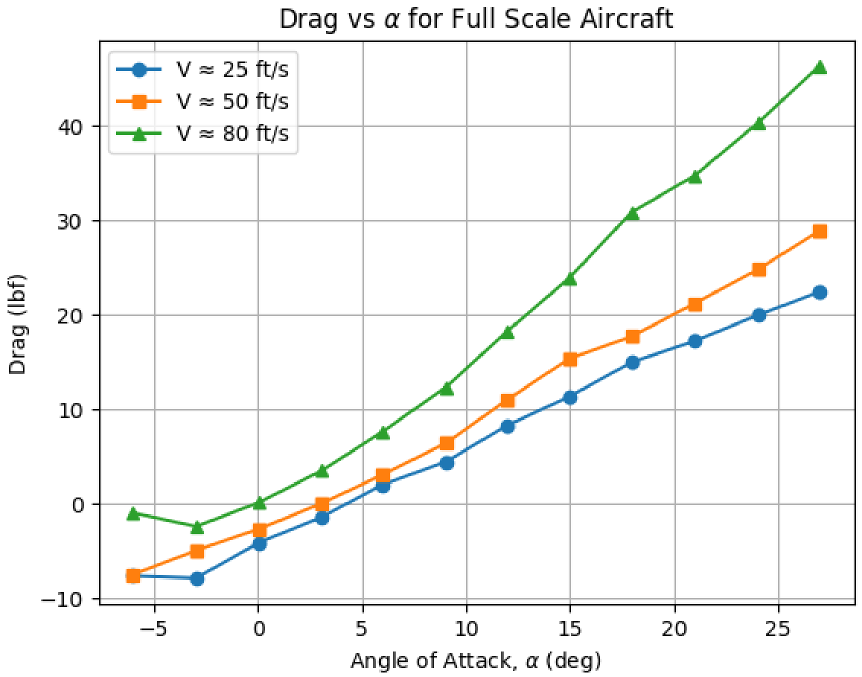

Figure 12: Predicted Drag versus Angle of Attack for the full-scale Aircraft

of 2 lb/ft^3 [9]. For rough estimates, we will assume that the carbon fiber skin will account for approximately 5 percent of the overall volume and the polystyrene foam will account for the remaining 95 percent of the volume. This is in itself an overestimate because a portion of the volume would be empty for payloads. These estimates give a rough estimated aircraft weight of 3.18 lbs.

The non-dimensional coefficients obtained from wind tunnel testing can be used to predict how the full-scale aircraft might perform. We can see the estimated lift values for the full-scale model in Fig. 11. Given the calculated lift values, we would likely want to fly our drone at around 50 ft/s, and at an angle of attack of around 3 to 7 degrees. This range puts the estimated lift at around 5 to 11 pounds, allowing a payload of 2 to 4 pounds on top of the estimated aircraft weight of roughly 3.2 pounds. This shows that our full-scale aircraft would likely be feasible for a launch condition of 50 ft/s and a low angle of attack.

Looking at predicted drag characteristics of the full-scale aircraft in Fig. 12, we can see that the aerodynamic drag increases roughly linearly with angle of attack, meaning that the aircraft would be able to use aerodynamic drag for braking during landing.

Overall, our wind tunnel tests suggest that our full-scale design is feasible and should move forward in the design process.

7 CONCLUSION

The experiment involved testing the aerodynamic performance of a blended-wing-body aircraft designed for small payload delivery by combining theoretical analysis with wind-tunnel testing of a scale model. AVL was used to predict characteristics like lift, drag, and moment based on the model's geometry. These predictions were compared to wind-tunnel measurements, specifically normal and axial forces and pitching moment, taken at freestream velocities of 25, 50 and 80 ft/s. From these data, values such as lift, drag, and moment coefficients were computed.

The experimental results showed that the lift coefficient increased approximately linearly with angle of attack pre-stall, and the drag coefficient followed a quadratic dependence. Both of these trends were expected. The neutral point estimates obtained for the faster wind tunnel speeds agreed with the AVL calculation based purely on geometry, indicating a slightly positive static stability margin. Polar drag was smooth across all Reynolds numbers tested, and the data were generally cleaner at higher wind tunnel speeds. The pitching-moment coefficient about the neutral point remained nearly constant for the higher speeds, indicating the design achieved near-neutral longitudinal stability as was desired for the flying-wing concept.

Scaling coefficients to a full-scale blended-wing-body, the results suggest that a similar aircraft with composite skin and foam-core could generate sufficient lift for a small payload. However, the significant Reynolds-number mismatch between the model and a full-scale aircraft, as well as the inviscid nature of AVL, limit the accuracy of drag and stall predictions. Overall, the experiment demonstrates that the team's blended-wing design is viable from an aerodynamic standpoint, and provides a springboard for future refinement and high-fidelity evaluation for a full-scale small payload delivery aircraft.

References

[1] Aviastar, “Westland Dreadnought,” `https://www.aviastar.org/air/england/west_dreadnought.php`, n.d.

[2] Larrimer, B., *Beyond Tube-and-Wing*, NASA Aeronautics Book Series, 2020.

[3] National Aeronautics and Space Administration, “Transformed X-48C Makes Successful First Flight,” `https://www.nasa.gov/news-release/transformed-x-48c-makes-successful-first-flight/`, 2013.

[4] Natilus, “The Evolution of Sustainable Air Freight,” `https://natilus.co/kona/#about`, n.d.

[5] Wired, “Drones Have Transformed Blood Delivery in Rwanda,” `https://www.wired.com/story/drones-have-transformed-blood-delivery-in-rwanda/`, 2022.

[6] University of Illinois at Urbana-Champaign, “Experiment #6: Design Lab,” Laboratory Note for AE 460, 2025, Department of Aerospace Engineering.

[7] Raymer, D. P., *Aircraft Design: A Conceptual Approach*, American Institute of Aeronautics and Astronautics, Reston, VA, 3rd ed., 1999.

[8] Toray Composite Materials America, Inc., “T300 Technical Data Sheet,” `https://www.toraycma.com/wp-content/uploads/T300-Technical-Data-Sheet-1.pdf`, 2025, Accessed: 9 December 2025.

[9] FoamByMail.com, “Polystyrene Foam Sheet,” `https://www.foambymail.com/polystyrene-foam-sheet.html`, 2025, Accessed: 9 December 2025.

APPENDIX A: SAMPLE CALCULATIONS

The code used to generate the plots in this report can be accessed with the following GitHub link:

Equation for full-scale Lift

$$L = qSC_L \tag{15}$$

$$q = \tfrac{1}{2}\rho V^2 \tag{16}$$

$$L = \tfrac{1}{2}(0.0022458307)(80.3533)^2(8.544)(0.4371) = 27.08 \text{ lbf} \tag{17}$$

Equation for full-scale Drag

$$D = qSC_D \tag{18}$$

$$D = \tfrac{1}{2}(0.0022458307)(80.3533)^2(8.544)(0.1237) = 7.66 \text{ lbf} \tag{19}$$

Equation for Reynolds Number

$$Re = \frac{\rho V c}{\mu} \tag{20}$$

$$c = \frac{1.31}{12} = 0.1092 \text{ ft} \tag{21}$$

$$Re = \frac{(0.0022458307)(80.3533)(0.1092)}{3.8123 \times 10^{-7}} = 5.17 \times 10^{4} \tag{22}$$

Equations for Lift Calculation

The lift is computed using the following equation:

$$L = N\cos\alpha - A\sin\alpha. \tag{23}$$

Let us use a data point from the flight test conducted at 25 ft/s. Substituting in these values, we find

$$L = (-0.001110)\cos(-0.1053) - (-0.044384)\sin(-0.1053). \tag{24}$$

Further simplifying the equation, we obtain

$$L = -0.001104 - 0.004660 = -0.00576 \text{ lbf}. \tag{25}$$

Equations for Drag Calculation

Drag is defined by

$$D = N\sin\alpha + A\cos\alpha. \tag{26}$$

Substituting in values from the 25 ft/s flight test, we find that

$$D = (-0.001110)(-0.1051) + (-0.044384)(0.99446), \tag{27}$$

$$D = 0.000117 - 0.04414 = -0.04402 \text{ lbf}. \tag{28}$$

Equations for Dynamic Pressure

Dynamic pressure is computed from the corrected pressure measurement:

$$q_\infty = 144\, q_{\text{corr}}. \tag{29}$$

This results in a dynamic pressure of

$$q_\infty = 144(0.0048129) = 0.6927 \text{ psf}. \tag{30}$$

Equations for Lift Coefficient

The lift coefficient is defined as

$$C_L = \frac{L}{q_\infty S}. \tag{31}$$

Substituting in the data, we see that

$$C_L = \frac{-0.00576}{(0.6927)(0.0498047)} = \frac{-0.00576}{0.03449} = -0.167. \tag{32}$$

Equations for Drag Coefficient

The equation for the drag coefficient is

$$C_D = \frac{D}{q_\infty S}. \tag{33}$$

Plugging in our data results in

$$C_D = \frac{-0.04402}{0.03449} = -1.277. \tag{34}$$

Equations for Pitching-Moment Coefficient About the Balance Center

The nondimensional pitching moment is

$$C_{M,\mathrm{bal}} = \frac{M_{\mathrm{bal}}}{q_\infty S\bar{c}}. \tag{35}$$

The denominator is computed as

$$q_\infty S\bar{c} = (0.6927)(0.0498047)(0.1125) = 0.00388. \tag{36}$$

Solving the entire equation results in

$$C_{M,\mathrm{bal}} = \frac{-0.005401}{0.00388} = -1.39. \tag{37}$$

Equations for Pitching-Moment Coefficient About the Neutral Point

The moment-arm difference is

$$dx = x_{\mathrm{ref}} - x_{NP} = 2.12 - 1.696 = 0.424 \text{ in.} \tag{38}$$

The nondimensional arm ratio is

$$\frac{dx}{\bar{c}} = \frac{0.424}{1.35} = 0.3148. \tag{39}$$

The lift-dependent correction term is

$$\left(\frac{dx}{\bar{c}}\right) C_L = (0.3148)(-0.167) = -0.0526. \tag{40}$$

Finally, the pitching-moment coefficient referenced to the neutral point is

$$C_m = C_{M,\text{bal}} - \left(\frac{dx}{\bar{c}}\right) C_L, \tag{41}$$

$$C_m = -1.39 - (-0.0526) = -1.34. \tag{42}$$

APPENDIX B: UNCERTAINTY ANALYSIS

Lift and Lift Coefficient Uncertainty

Given (V=80ft/s):

- $L = 0.00441068$ lbf
- $C_L = 0.01224036777$
- $\alpha = -6.03094^\circ = -0.10526$ rad
- Normal force: $N = -0.0886903$ lbf, $\sigma_N = 0.00443451$ lbf
- Axial force: $A = -0.0146314$ lbf, $\sigma_A = 0.00073157$ lbf
- Angle uncertainty: $\sigma_\alpha = 0.0034907$ rad

1) Lift uncertainty:

$$\sigma_L = \sqrt{\left(\frac{\partial L}{\partial N}\sigma_N\right)^2 + \left(\frac{\partial L}{\partial A}\sigma_A\right)^2 + \left(\frac{\partial L}{\partial \alpha}\sigma_\alpha\right)^2} \tag{43}$$

Where the partial derivatives are:

$$\frac{\partial L}{\partial N} = \cos\alpha, \quad \frac{\partial L}{\partial A} = -\sin\alpha, \quad \frac{\partial L}{\partial \alpha} = -N\sin\alpha + A\cos\alpha \tag{44}$$

Substitute numerical values:

$$\begin{aligned}\sigma_L = \surd&(\cos(-0.105)\cdot 0.004)^2\\ &+(-\sin(-0.105)\cdot 0.001)^2\\ &+\Big((-(-0.089)\sin(-0.105)+(-0.015)\cos(-0.105))\cdot 0.003\Big)^2\end{aligned}\tag{45}$$

$$\sigma_L \approx 0.00441 \text{ lbf} \tag{46}$$

2) Lift coefficient uncertainty:

$$\sigma_{C_L} = C_L\frac{\sigma_L}{L} \tag{47}$$

$$\sigma_{C_L} = 0.01224036777\cdot\frac{0.00441}{0.00441068} \approx 0.01224 \tag{48}$$

.1 Drag and Drag Coefficient Uncertainty

Given (V = 80 ft/s):

- $D = -0.015$ lbf
- $C_D = -0.005$
- $\alpha = -6.031^\circ = -0.105$ rad
- Normal force: $N = -0.0887$ lbf, $\sigma_N = 0.004$ lbf
- Axial force: $A = -0.015$ lbf, $\sigma_A = 0.001$ lbf
- Angle uncertainty: $\sigma_\alpha = 0.003$ rad
- Drag uncertainty: $\sigma_D = 0.001$ lbf

1) Drag coefficient uncertainty:

$$\begin{aligned}\sigma_{C_D} &= C_D \frac{\sigma_D}{D} \\ &= -0.005 \cdot \frac{0.001}{-0.015} \\ &\approx 0.0025 \end{aligned} \tag{49}$$

APPENDIX C: COMPUTER PROGRAMS

The code used to generate the plots in this report can be accessed with the following GitHub link: `AE 460 Design Lab Repository`

APPENDIX D: RAW DATA

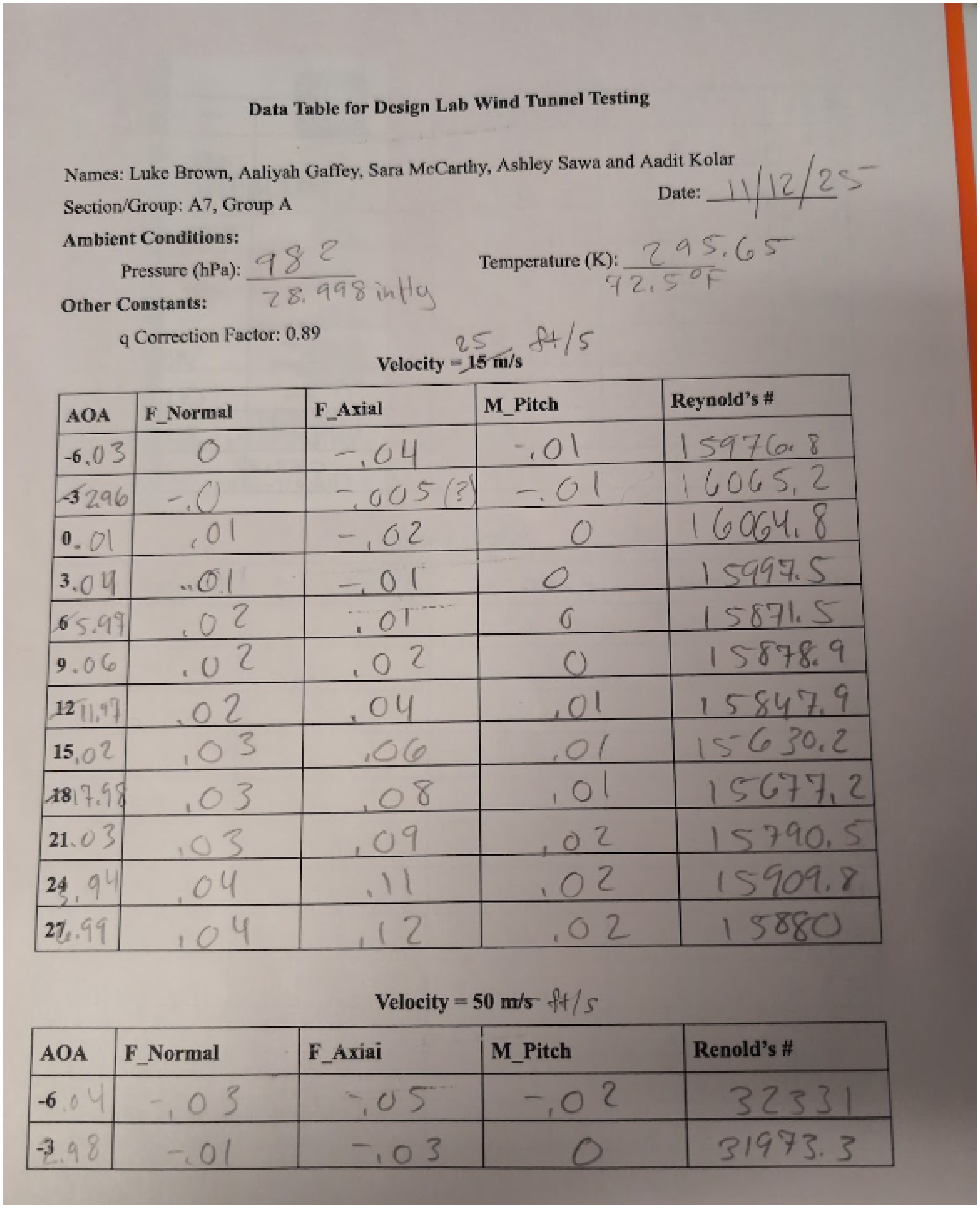

Data Table for Design Lab Wind Tunnel Testing

Names: Luke Brown, Aaliyah Gaffey, Sara McCarthy, Ashley Sawa and Aadit Kolar

Section/Group: A7, Group A

Date: 11/12/25

Ambient Conditions:

Pressure (hPa): 982
28.998 inHg

Temperature (K): 295.65
72.5°F

Other Constants:

q Correction Factor: 0.89

Velocity = ~~15~~ 25 ~~m/s~~ ft/s

AOA	F_Normal	F_Axial	M_Pitch	Reynold's #
-6.03	0	-.04	-.01	15976.8
~~-3~~ 2.96	-.0	-.005 (?)	-.01	16065.2
0.01	.01	-.02	0	16064.8
3.04	-.01	-.01	0	15997.5
~~6~~ 5.99	.02	.01	0	15871.5
9.06	.02	.02	0	15878.9
~~12~~ 11.97	.02	.04	.01	15847.9
15.02	.03	.06	.01	15630.2
~~18~~ 17.98	.03	.08	.01	15677.2
21.03	.03	.09	.02	15790.5
2~~4~~3.94	.04	.11	.02	15909.8
2~~7~~6.99	.04	.12	.02	15880

Velocity = 50 ~~m/s~~ ft/s

AOA	F_Normal	F_Axiai	M_Pitch	Renold's #
-6.04	-.03	-.05	-.02	32331
-~~3~~2.98	-.01	-.03	0	31973.3

Figure 13: First Page of Handwritten Data

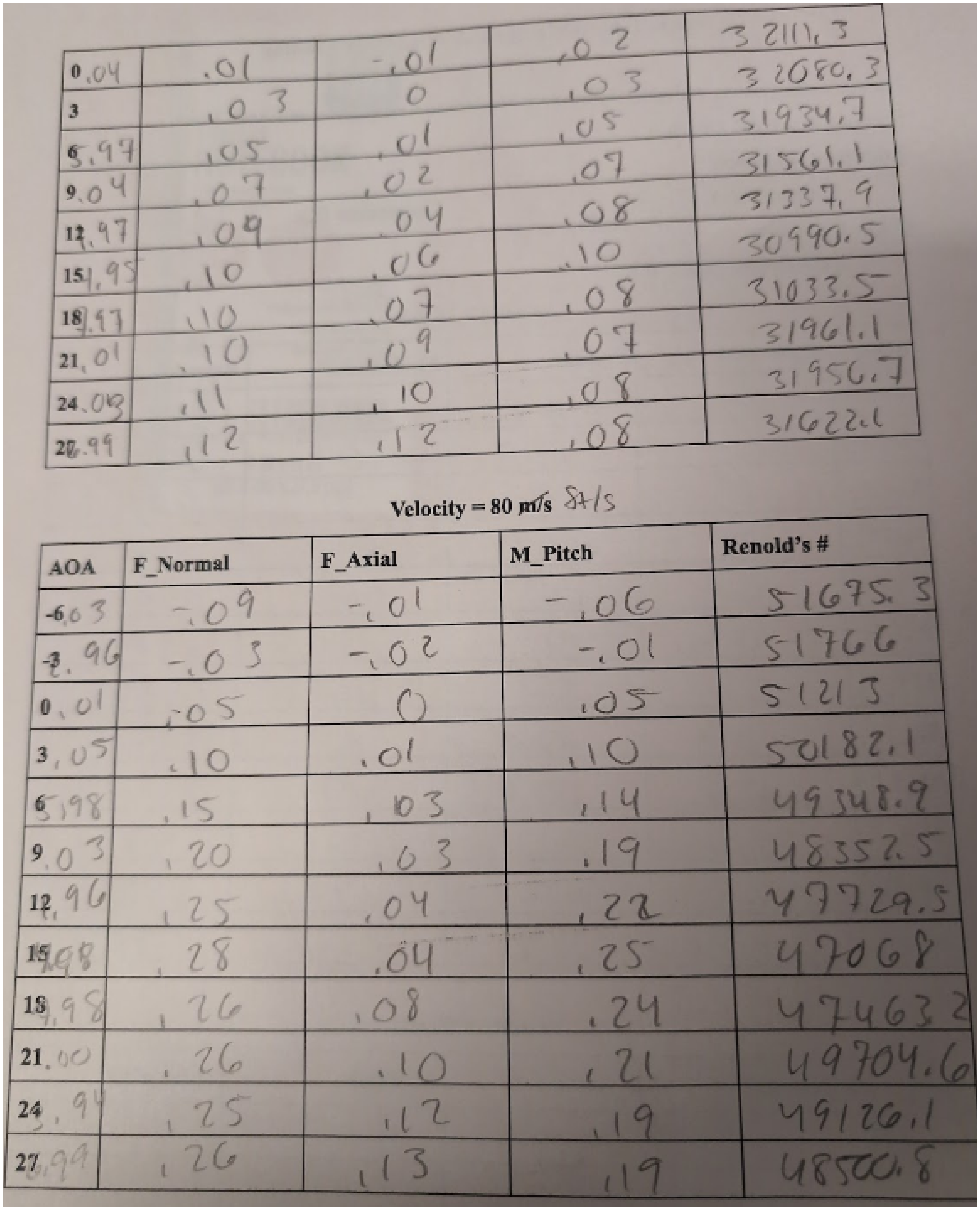

0.04	.01	-.01	.02	32111.3
3	.03	0	.03	32080.3
5.97	.05	.01	.05	31934.7
9.04	.07	.02	.07	31561.1
11.97	.09	.04	.08	31337.9
14.95	.10	.06	.10	30990.5
17.97	.10	.07	.08	31033.5
21.01	.10	.09	.07	31961.1
24.03	.11	.10	.08	31956.7
26.99	.12	.12	.08	31622.1

Velocity = 80 ~~m~~/s ft/s

AOA	F_Normal	F_Axial	M_Pitch	Renold's #
-6.03	-.09	-.01	-.06	51675.3
-2.96	-.03	-.02	-.01	51766
0.01	.05	0	.05	51213
3.05	.10	.01	.10	50182.1
5.98	.15	.03	.14	49348.9
9.03	.20	.03	.19	48352.5
12.96	.25	.04	.22	47729.5
14.98	.28	.04	.25	47068
17.98	.26	.08	.24	47463.2
21.00	.26	.10	.21	49704.6
23.94	.25	.12	.19	49126.1
26.99	.26	.13	.19	48500.8

Figure 14: Second Page of Handwritten Data

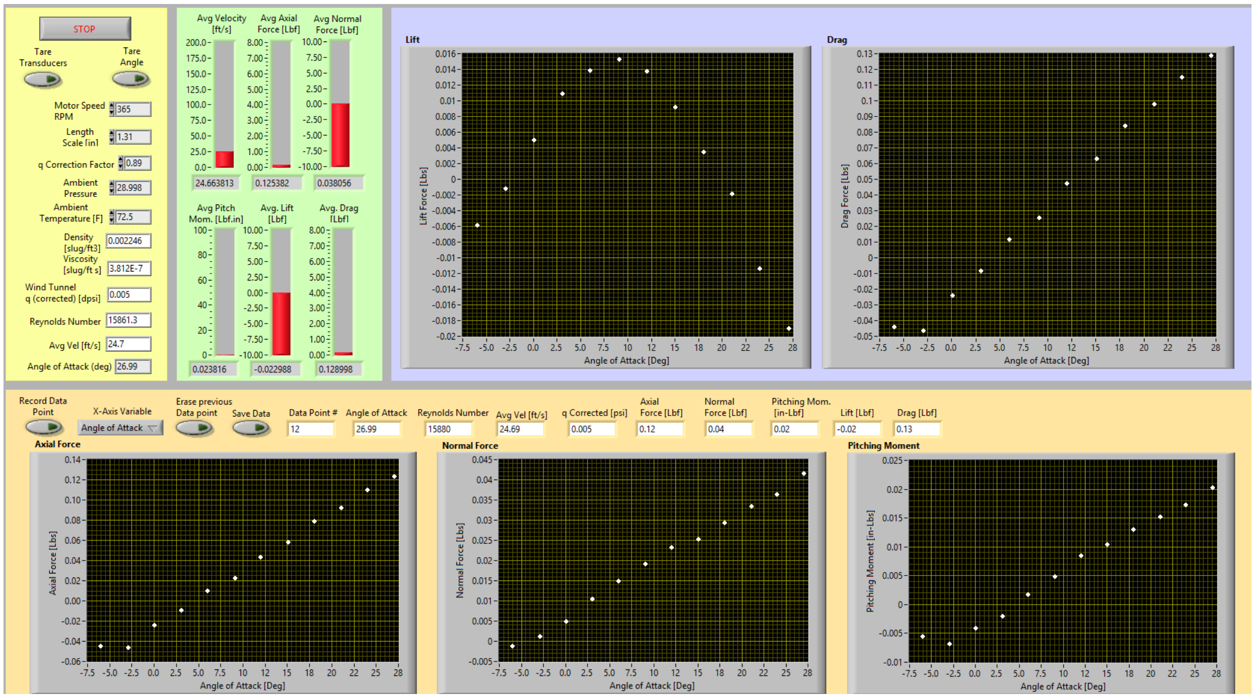
Motor Speed RPM: 365
Length Scale [in]: 1.31
q Correction Factor: 0.89
Ambient Pressure: 28.998
Ambient Temperature [F]: 72.5
Density [slug/ft3]: 0.002246
Viscosity [slug/ft s]: 3.812E-7
Wind Tunnel q (corrected) [dpsi]: 0.005
Reynolds Number: 15861.3
Avg Vel [ft/s]: 24.7
Angle of Attack (deg): 26.99
Avg Velocity [ft/s]: 24.663813
Avg Axial Force [Lbf]: 0.125382
Avg Normal Force [Lbf]: 0.038056
Avg Pitch Mom. [Lbf.in]: 0.023816
Avg. Lift [Lbf]: -0.022988
Avg. Drag [Lbf]: 0.128998
X-Axis Variable: Angle of Attack

Data Point #	Angle of Attack	Reynolds Number	Avg Vel [ft/s]	q Corrected [psi]	Axial Force [Lbf]	Normal Force [Lbf]	Pitching Mom. [in-Lbf]	Lift [Lbf]	Drag [Lbf]
12	26.99	15880	24.69	0.005	0.12	0.04	0.02	-0.02	0.13

Figure 15: Various Graphs for 25 ft/s

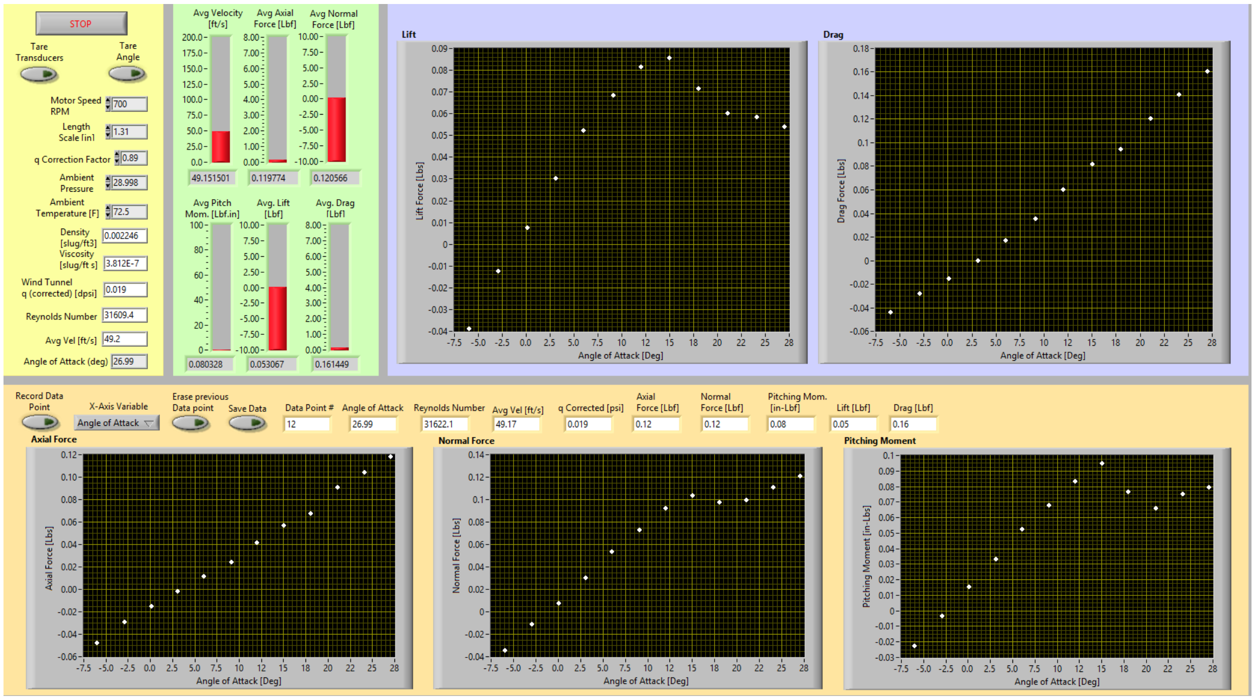
Motor Speed RPM: 700
Length Scale [in]: 1.31
q Correction Factor: 0.89
Ambient Pressure: 28.998
Ambient Temperature [F]: 72.5
Density [slug/ft3]: 0.002246
Viscosity [slug/ft s]: 3.812E-7
Wind Tunnel q (corrected) [dpsi]: 0.019
Reynolds Number: 31609.4
Avg Vel [ft/s]: 49.2
Angle of Attack (deg): 26.99
Avg Velocity [ft/s]: 49.151501
Avg Axial Force [Lbf]: 0.119774
Avg Normal Force [Lbf]: 0.120566
Avg Pitch Mom. [Lbf.in]: 0.080328
Avg. Lift [Lbf]: 0.053067
Avg. Drag [Lbf]: 0.161449
X-Axis Variable: Angle of Attack

Data Point #	Angle of Attack	Reynolds Number	Avg Vel [ft/s]	q Corrected [psi]	Axial Force [Lbf]	Normal Force [Lbf]	Pitching Mom. [in-Lbf]	Lift [Lbf]	Drag [Lbf]
12	26.99	31622.1	49.17	0.019	0.12	0.12	0.08	0.05	0.16

Figure 16: Various Graphs for 50 ft/s

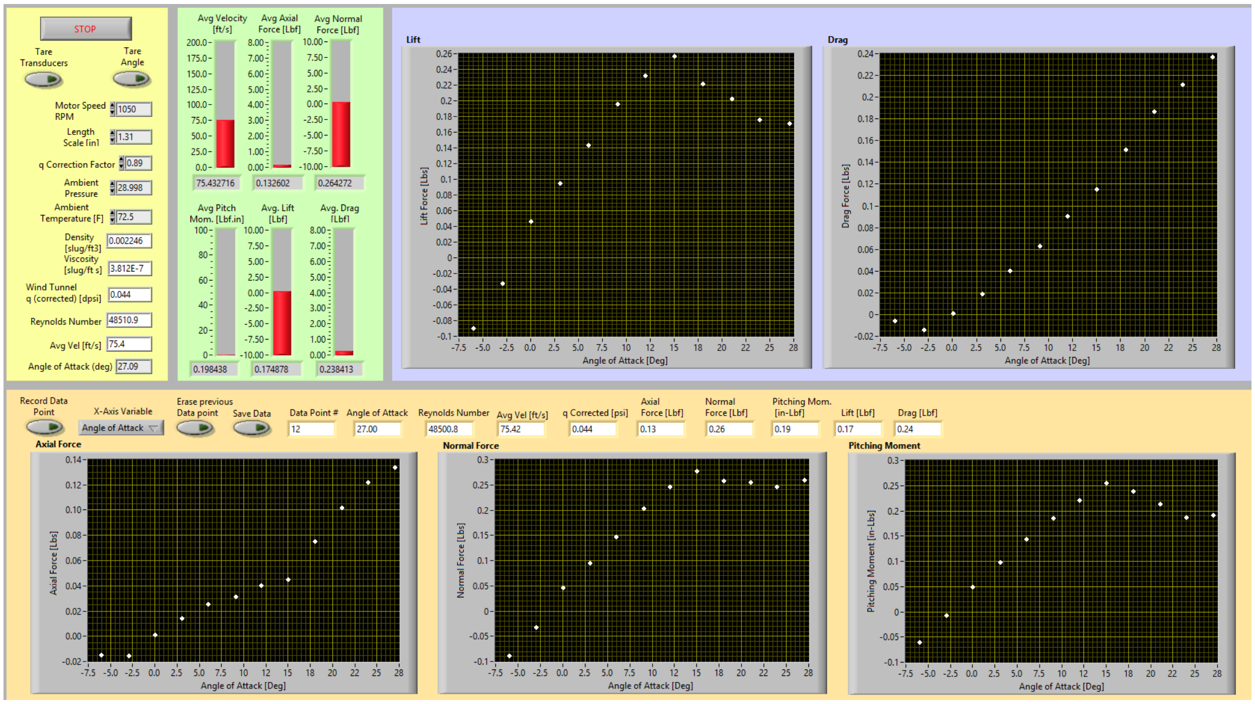

Motor Speed RPM: 1050
Length Scale [in]: 1.31
q Correction Factor: 0.89
Ambient Pressure: 28.998
Ambient Temperature [F]: 72.5
Density [slug/ft3]: 0.002246
Viscosity [slug/ft s]: 3.812E-7
Wind Tunnel q (corrected) [dpsi]: 0.044
Reynolds Number: 48510.9
Avg Vel [ft/s]: 75.4
Angle of Attack (deg): 27.09

Avg Velocity [ft/s]: 75.432716
Avg Axial Force [Lbf]: 0.132602
Avg Normal Force [Lbf]: 0.264272
Avg Pitch Mom. [Lbf.in]: 0.198438
Avg. Lift [Lbf]: 0.174878
Avg. Drag [Lbf]: 0.238413

X-Axis Variable: Angle of Attack

Data Point #	Angle of Attack	Reynolds Number	Avg Vel [ft/s]	q Corrected [psi]	Axial Force [Lbf]	Normal Force [Lbf]	Pitching Mom. [in-Lbf]	Lift [Lbf]	Drag [Lbf]
12	27.00	48500.8	75.42	0.044	0.13	0.26	0.19	0.17	0.24

Figure 17: Various Graphs for 80 ft/s

Table 7: Data for 80 ft/s

Data Point	Corr Factor	Length Scale [in]	AmbPress [psia]	AmbTemp [R]	Density [slug/ft^3]	Viscosity [slug/ft s]	Motor Speed [RPM]	AoA [deg]	Corrected q [dpsi]	Avg Velocity [ft/s]	Reynolds No.	Axial Force [Lbf]	Normal Force [Lbf]	Pitching Mom [in-Lbf]
1	0.89	1.31	14.2423677	532.17	0.0022458307	0.00000038123	1050	-6.030942135	0.05034915715	80.35332489	51675.33203	-0.01463136738	-0.08869029963	-0.05935735364
2	0.89	1.31	14.2423677	532.17	0.0022458307	0.00000038123	1050	-2.964423842	0.05052604144	80.49434662	51766.02344	-0.01529658957	-0.03123886925	-0.00612517433
3	0.89	1.31	14.2423677	532.17	0.0022458307	0.00000038123	1050	0.00921183733	0.04945233001	79.63447571	51213.03906	0.001054249	0.04672222963	0.04971069583
4	0.89	1.31	14.2423677	532.17	0.0022458307	0.00000038123	1050	3.045460716	0.0474813022	78.03133392	50182.05859	0.01438784904	0.09602314974	0.09847603685
5	0.89	1.31	14.2423677	532.17	0.0022458307	0.00000038123	1050	5.980051852	0.04591767438	76.73574066	49348.85938	0.02545778258	0.1471024257	0.1447955676
6	0.89	1.31	14.2423677	532.17	0.0022458307	0.00000038123	1050	9.033810045	0.04408229514	75.18649292	48352.53516	0.03158844414	0.2034333086	0.1861127
7	0.89	1.31	14.2423677	532.17	0.0022458307	0.00000038123	1050	11.96318796	0.04295352452	74.21763611	47729.46484	0.04048424827	0.2463706588	0.2208501734
8	0.89	1.31	14.2423677	532.17	0.0022458307	0.00000038123	1050	14.97817456	0.04177123732	73.18910217	47068.01172	0.04499355869	0.278308622	0.2548700145
9	0.89	1.31	14.2423677	532.17	0.0022458307	0.00000038123	1050	17.98242083	0.04247565935	73.80364227	47463.22266	0.07562132203	0.2581659217	0.2392116984
10	0.89	1.31	14.2423677	532.17	0.0022458307	0.00000038123	1050	21.00432654	0.04658203885	77.28887177	49704.57813	0.1021131733	0.2562573972	0.2138895754
11	0.89	1.31	14.2423677	532.17	0.0022458307	0.00000038123	1050	23.93546494	0.04550412397	76.3894043	49126.13281	0.1224121335	0.2466339272	0.1868634979
12	0.89	1.31	14.2423677	532.17	0.0022458307	0.00000038123	1050	26.99692013	0.04435295826	75.41696167	48500.75	0.1338205861	0.2605649558	0.1923186269

Table 8: Data for 50 ft/s

Data Point	Corr Factor	Length Scale [in]	AmbPress [psia]	AmbTemp [R]	Density [slug/ft^3]	Viscosity [slug/ft s]	Motor Speed [RPM]	AoA [deg]	Corrected q [dpsi]	Avg Velocity [ft/s]	Reynolds No.	Axial Force [Lbf]	Normal Force [Lbf]	Pitching Mom [in-Lbf]
1	0.89	1.31	14.2423677	532.17	0.0022458307	0.00000038123	700	-6.035554878	0.01970897516	50.27357483	32331.00586	-0.04712684754	-0.03386524403	-0.02236076679
2	0.89	1.31	14.2423677	532.17	0.0022458307	0.00000038123	700	-2.980418321	0.01927533107	49.71743011	31973.34766	-0.02837139651	-0.01066366433	-0.00320511913
3	0.89	1.31	14.2423677	532.17	0.0022458307	0.00000038123	700	0.0397405486	0.01944208116	49.93201828	32111.34961	-0.01497278004	0.00796361077	0.01550314203
4	0.89	1.31	14.2423677	532.17	0.0022458307	0.00000038123	700	3.051096996	0.01940450473	49.88373947	32080.30078	-0.00114106672	0.03044606842	0.03340679322
5	0.89	1.31	14.2423677	532.17	0.0022458307	0.00000038123	700	5.974797693	0.01922880858	49.65739441	31934.73828	0.01213340356	0.05401181437	0.05293215171
6	0.89	1.31	14.2423677	532.17	0.0022458307	0.00000038123	700	9.038095255	0.01878143589	49.07633591	31561.05859	0.02460951905	0.07355964956	0.06822362488
7	0.89	1.31	14.2423677	532.17	0.0022458307	0.00000038123	700	11.96803271	0.01851680337	48.72936249	31337.91992	0.04207020829	0.09244344667	0.08367095736
8	0.89	1.31	14.2423677	532.17	0.0022458307	0.00000038123	700	14.95321389	0.01810853972	48.18917084	30990.52148	0.05729793697	0.1042145458	0.0953745338
9	0.89	1.31	14.2423677	532.17	0.0022458307	0.00000038123	700	17.97121651	0.01815874646	48.25592804	31033.45313	0.06830151749	0.09775108148	0.07699164273
10	0.89	1.31	14.2423677	532.17	0.0022458307	0.00000038123	700	21.00678303	0.01926053413	49.69834137	31961.07227	0.09112546828	0.09981196126	0.06651949034
11	0.89	1.31	14.2423677	532.17	0.0022458307	0.00000038123	700	24.03158193	0.0192552973	49.69158554	31956.72656	0.104945259	0.1110398513	0.07522576978
12	0.89	1.31	14.2423677	532.17	0.0022458307	0.00000038123	700	26.99184339	0.01885410263	49.17118454	31622.05664	0.1187559424	0.1214430019	0.07996612382

Table 9: Data for 25 ft/s

Data Point	Corr Factor	Length Scale [in]	AmbPress [psia]	AmbTemp [R]	Density [slug/ft^3]	Viscosity [slug/ft s]	Motor Speed [RPM]	AoA [deg]	Corrected q [dpsi]	Avg Velocity [ft/s]	Reynolds No.	Axial Force [Lbf]	Normal Force [Lbf]	Pitching Mom [in-Lbf]
1	0.89	1.31	14.2423677	532.17	0.0022458307	0.00000038123	365	-6.032306852	0.00481289328	24.84338951	15976.81836	-0.04438406435	-0.00111019192	-0.00540085392
2	0.89	1.31	14.2423677	532.17	0.0022458307	0.00000038123	365	-2.964628549	0.00486629504	24.98083496	16065.20898	-0.04595188802	0.00124010723	-0.0068139269
3	0.89	1.31	14.2423677	532.17	0.0022458307	0.00000038123	365	0.00944383916	0.00486606041	24.98023224	16064.82129	-0.02385848868	0.00507977009	-0.00408392312
4	0.89	1.31	14.2423677	532.17	0.0022458307	0.00000038123	365	3.036139701	0.00482538381	24.87560654	15997.53711	-0.00852525494	0.01046978246	-0.0020060564
5	0.89	1.31	14.2423677	532.17	0.0022458307	0.00000038123	365	5.974661221	0.00474963687	24.67959023	15871.47852	0.01032507243	0.01502770296	0.00181372444
6	0.89	1.31	14.2423677	532.17	0.0022458307	0.00000038123	365	9.057133052	0.00475405498	24.69106674	15878.85938	0.02313686322	0.01924606812	0.00488859129
7	0.89	1.31	14.2423677	532.17	0.0022458307	0.00000038123	365	11.967828	0.00473551888	24.6428833	15847.87207	0.04379046687	0.02337560739	0.00847992733
8	0.89	1.31	14.2423677	532.17	0.0022458307	0.00000038123	365	15.02183184	0.00460633024	24.30442047	15630.20605	0.05874876662	0.02535138721	0.01043692054
9	0.89	1.31	14.2423677	532.17	0.0022458307	0.00000038123	365	17.98285754	0.00463409197	24.37755013	15677.23633	0.07896578976	0.02935372861	0.01303027226
10	0.89	1.31	14.2423677	532.17	0.0022458307	0.00000038123	365	21.02792249	0.00470126726	24.55360222	15790.45508	0.092245905	0.03350260291	0.01528457072
11	0.89	1.31	14.2423677	532.17	0.0022458307	0.00000038123	365	23.935192	0.00477262604	24.73924446	15909.8418	0.1100406343	0.03641161093	0.01738291461
12	0.89	1.31	14.2423677	532.17	0.0022458307	0.00000038123	365	26.99401329	0.00475473892	24.69284248	15880.00098	0.1236321886	0.04175787606	0.02030270525

APPENDIX E: GROUP MEMBER CONTRIBUTIONS

Group Member	**Contribution to Technical Note**
Sara	Apparatus, Procedure, Tabulated Data, & Raw Data
Ashley	Neutral Point Calculations, Engineering Drawing, & Conclusion
Aaliyah	Abstract, Introduction, Theory & Analysis, Aerodynamic Data
Luke	Experimental Uncertainty & full-scale Aircraft Analysis
Aadit	Description of Design & Theoretical Analysis